Comparison of electronic band structure and optical transparency conditions of $In_xGa_{1-x}As_{1-y}N_y$/GaAs quantum wells calculated by 10-band, 8-band, and 6-band k·p models

S. T. Ng, W. J. Fan, Y. X. Dang, and S. F. Yoon

School of Electrical and Electronic Engineering, Nanyang Technological University, Singapore 639798
(Received 16 September 2004; revised manuscript received 18 July 2005; published 28 September 2005)

We have investigated the electronic band structure and optical transparency conditions of $In_xGa_{1-x}As_{1-y}N_y$/GaAs quantum well (QW) using 10-band, 8-band and 6-band **k·p** models. The transition energy calculated by the 8-band model agrees very well with the values calculated by the 10-band model, especially in the range of high indium composition (35%). Electron effective mass (m_e^*) predicated by band anticrossing model, with nitrogen-related enhancement weakened as indium composition increases, was used in the 8-band model and was favored compared to the heavier value predicted by the phenomenological relationship. We have calculated the optical transition matrix element ($Q_i^{n_cn_v}$) using the Bloch wave functions for the **k·p** models and discovered that the inclusion of nitrogen-related energy level (E_N) into the calculation of the conduction band by the 10-band **k·p** model yields lower differential gain (dG/dN) than that calculated by the 8-band **k·p** model on the same structure. Contrary to earlier reports that the reduction of dG/dN in $In_xGa_{1-x}As_{1-y}N_y$/GaAs QW and thus the lower obtainable optical gain is due to the increase in m_e^*, we have concluded that the reduction was due to the increased interaction between the $|S\rangle$ conduction-band state and $|S_N\rangle$ nitrogen-related energy state, which weaken the optical transition matrix elements between valence band and conduction band. Our results also show that if m_e^* is very large (as predicted by the phenomenological model), dG/dN will increase monotonously with nitrogen composition. Moreover, neglecting valence band and conduction band interaction in **k·p** models will result in the prediction of higher dG/dN which is not accurate.

I. INTRODUCTION

Ever since the InGaAsN/GaAs material was introduced as a possible candidate to replace InGaAsP/InP material as the conventional long-wavelength laser emitter and detector,[1] it has continued to attract attention from the research community. Not only that samples were grown by both molecular beam epitaxy (MBE) and metal organic chemical vapor deposition (MOCVD) to explore the possibility of achieving 1.3 μm (Refs. 2–10) and near 1.55 μm (Refs. 11–18) emission, but also various theories were proposed in an attempt to predict the compositional dependence of the $In_xGa_{1-x}As_{1-y}N_y$ bulk material. The $In_xGa_{1-x}As$/GaAs quantum well (QW) has been shown to exhibit very low threshold current density due to the presence of compressive strain in the well layer under lattice mismatch.[19,20] However, the compressive strain will build up when more indium are being added to the well layer to increase the emission wavelength and thus imposed a limit to the thickness of the QW. By adding nitrogen atom into the matrix to form $In_xGa_{1-x}As_{1-y}N_y$/GaAs, it was found to further reduce the band gap energy and simultaneously reduce the compressive strain present in the well layer. This special material exhibits very different behaviors, including the larger than normal band gap bowing factor and enhancement of electron effective mass (m_e^*) by the addition of a nitrogen atom.

The dependence of band gap energy (E_G) on nitrogen composition has been predicted very well by the band anticrossing (BAC) model, which states that the large reduction of the fundamental band gap energy of $In_xGa_{1-x}As_{1-y}N_y$ is due to the repulsion between a localized nitrogen-related en-

ergy level (E_N) and the extended conduction band (E_C) of the $In_xGa_{1-x}As$ host matrix.[21] To date, the BAC model is used extensively and successfully in the prediction of E_G of $In_xGa_{1-x}As_{1-y}N_y$ with low indium composition and $GaAs_{1-y}N_y$.[21–23] However, it was discovered that the interaction between E_N and E_C depends not only on the nitrogen composition, but it is also a function of indium composition. Consequently, the rate of reduction of band gap energy with respect to nitrogen composition (dE_G/dy) decreases when the indium composition increases, as the downward shift of E_C with respect to valence band maximum is greater than that of E_N.[24] Therefore, the next question is whether m_e^* in the conduction band is showing the same kind of weakened dependence on nitrogen composition when indium composition in the well layer is being increased. This is important to study since the technologically important 1.3 μm emission will require the indium composition to be in the range of 30% to 40%. The validity of this weakened enhancement will undoubtedly affect the prediction of transparency conditions of QWs, which will be assessed in this paper.

In order to understand the performance figure of $In_xGa_{1-x}As_{1-y}N_y$/GaAs system, various studies have been undertaken using **k·p** method, which include, the performance of InGaAsN/GaAs semiconductor optical amplifiers emitting at 1.3 μm (with 6-band model in the valence band plus BAC in the conduction band),[25] the comparison of material gain of InGaAsN/GaAs with InGaAsP/InGaAsP and InGaAs/AlInGaAs (4-band model in the valence band plus BAC in the conduction band),[26] nitrogen-induced modification to the gain characteristics (10-band for both valence and conduction bands),[27,28] interdiffusion in InGaAsN/GaAs

QW (8-band model with phenomenological m_e^*),[29] and also the effect of adding nitrogen into the GaAs barrier (6-band model in the valence band and single band in the conduction band).[30] Despite the saving on computing requirement by using various assumptions to simplify the simulation, either by flattening of the band structure using large m_e^* or neglecting valence band (VB) and conduction band (CB) interaction, we are aware that these simplified $\mathbf{k} \cdot \mathbf{p}$ models (other than the 10-band model) may not give an accurate prediction of the real properties. We are not sure whether the presence of VB and CB interaction will yield different results to some of the findings in these literatures, or whether a heavier m_e^* predicted by phenomenological model[31] will be able to give agreeable results with the supposedly most complete and realistic 10-band $\mathbf{k} \cdot \mathbf{p}$ model. Therefore, it is of great importance that these doubts be clarified to ascertain that whether simplified models are to be used for future investigation of material properties on III-*N-V* compounds.

In this paper, we give a detail description of the various $\mathbf{k} \cdot \mathbf{p}$ formalisms, which include different combination of bands considered in the model, and compared their results to determine if there is any obvious discrepancy in the results. Section II will highlight the method that was used to compute the band structure and optical properties of InGaAsN/GaAs QW, including the choice of nitrogen-related band parameters. Section III will focus on the results calculated by different formalisms and the effect of neglecting VB and CB interaction and using heavier m_e^* on the prediction of transition energy and optical transparency conditions. Section IV will give an overall conclusion for this study.

II. METHOD

A. 8-band model

The 8-band Hamiltonian for strained bulk semiconductor, which takes into account the energy levels from conduction band (CB), heavy hole (hh), light hole (lh), and spin-orbit split-off (so) bands, is given below[32]

$$
H_k + H_s =
\begin{bmatrix}
C & 0 & -\frac{1}{\sqrt{2}}P_+ & \sqrt{\frac{2}{3}}P_z & \frac{1}{\sqrt{6}}P_- & 0 & \frac{1}{\sqrt{3}}P_z & \frac{1}{\sqrt{3}}P_- \\
0 & C & 0 & -\frac{1}{\sqrt{6}}P_+ & \sqrt{\frac{2}{3}}P_z & \frac{1}{\sqrt{2}}P_- & \frac{1}{\sqrt{3}}P_+ & -\frac{1}{\sqrt{3}}P_z \\
-\frac{1}{\sqrt{2}}P_+^* & 0 & H & \alpha & \beta & 0 & i\frac{\alpha}{\sqrt{2}} & -i\sqrt{2}\beta \\
\sqrt{\frac{2}{3}}P_z & -\frac{1}{\sqrt{6}}P_+^* & \alpha^* & L & 0 & \beta & i\left(\sqrt{2}\varepsilon - \frac{D}{\sqrt{2}}\right) & i\sqrt{\frac{3}{2}}\alpha \\
\frac{1}{\sqrt{6}}P_-^* & \sqrt{\frac{2}{3}}P_z & \beta^* & 0 & L & -\alpha & -i\sqrt{\frac{3}{2}}\alpha^* & i\left(\sqrt{2}\varepsilon - \frac{D}{\sqrt{2}}\right) \\
0 & \frac{1}{\sqrt{2}}P_-^* & 0 & \beta^* & -\alpha^* & H & -i\sqrt{2}\beta^* & -i\frac{\alpha^*}{\sqrt{2}} \\
\frac{1}{\sqrt{3}}P_z & \frac{1}{\sqrt{3}}P_+^* & -i\frac{\alpha^*}{\sqrt{2}} & i\left(\frac{D}{\sqrt{2}} - \sqrt{2}\varepsilon\right) & i\sqrt{\frac{3}{2}}\alpha & i\sqrt{2}\beta & S & 0 \\
\frac{1}{\sqrt{3}}P_-^* & -\frac{1}{\sqrt{3}}P_z & i\sqrt{2}\beta^* & -i\sqrt{\frac{3}{2}}\alpha^* & i\left(\frac{D}{\sqrt{2}} - \sqrt{2}\varepsilon\right) & i\frac{\alpha}{\sqrt{2}} & 0 & S
\end{bmatrix},
\tag{1}
$$

where

$$
C = E_G + \varepsilon_1(z) + \frac{\hbar^2}{2m_0}\left[\frac{1}{m_e^*} - \frac{E_P}{3}\left(\frac{2}{E_G} + \frac{1}{E_G + \Delta}\right)\right]
$$
$$
\times (k_x^2 + k_y^2 + k_z^2),
$$

$$
H = -\frac{\hbar^2}{2m_0}[(k_x^2 + k_y^2)(\gamma_1 + \gamma_2) + k_z^2(\gamma_1 - 2\gamma_2)] + \varepsilon_2(z),
$$

$$
L = -\frac{\hbar^2}{2m_0}[(k_x^2 + k_y^2)(\gamma_1 - \gamma_2) + k_z^2(\gamma_1 + 2\gamma_2)] - \varepsilon_2(z),
$$

$$
S = -\frac{\hbar^2}{2m_0}[(k_x^2 + k_y^2 + k_z^2)\gamma_1] - \Delta,
$$

$$
P_\pm = P(k_x \pm ik_y) - P(e_{xx}k_x \pm ie_{yy}k_y),
$$

$$
P_z = Pk_z - P(e_{zz}k_z),
$$

$$\alpha = -\frac{\hbar^2}{2m_0}2\sqrt{3}[k_z(ik_y - k_x)\gamma_3],$$

$$\beta = -\frac{\hbar^2}{2m_0}\sqrt{3}[2ik_xk_y\gamma_3 - (k_x^2 - k_y^2)\gamma_2],$$

$$D = -\frac{\hbar^2}{2m_0}[2(k_x^2 - k_y^2)\gamma_2 - 4k_z^2\gamma_2],$$

$$\varepsilon_1(z) = \begin{cases} 2(a_c + a_v)(1 - c_{12}/c_{11})e_{xx}, & \text{in the well,} \\ 0, & \text{in the barrier,} \end{cases}$$

$$\varepsilon_2(z) = \begin{cases} b(1 + 2c_{12}/c_{11})e_{xx}, & \text{in the well,} \\ 0, & \text{in the barrier.} \end{cases} \quad (2)$$

E_G is the unstrained band gap of the material. Δ is the spin-orbit splitting energy. a_c and a_v are the hydrostatic deformation potential for conduction and valence band, respectively. b is the shear deformation potential. c_{11} and c_{12} are the elastic stiffness constants. $e_{xx} = (a_s - a_w)/a_w$ is the in-plane strain, a_s and a_w are the lattice constants for the substrate and well layer, respectively. $e_{zz} = -2c_{12}/c_{11}e_{xx}$ is the strain in the perpendicular direction. P is the Kane matrix element and is normally expressed in terms of energy units as[33,34]

$$E_P = \frac{2m_0}{\hbar^2}P^2. \quad (3)$$

The valence band parameters $(\gamma_1, \gamma_2, \gamma_3)$ used in the 8-band Hamiltonian is not identical to Luttinger parameters $(\gamma_1^L, \gamma_2^L, \gamma_3^L)$ used in 6-band Hamiltonian, since the conduction band is now treated exactly in the 8-band Hamiltonian and must be subtracted off the original Luttinger parameters.[35] These parameters are called modified Luttinger parameters and are related to Luttinger parameters in the following manner:[32,35,36]

$$\gamma_1 = \gamma_1^L - \frac{1}{3}\frac{E_P}{E_G},$$

$$\gamma_2 = \gamma_2^L - \frac{1}{6}\frac{E_P}{E_G},$$

$$\gamma_3 = \gamma_3^L - \frac{1}{6}\frac{E_P}{E_G}. \quad (4)$$

The total Hamiltonian for strained QW is given by

$$H = H_k + H_s + V(z), \quad (5)$$

where, $V(z)$ describes the conduction and valence band off-set.

The eight-dimensional electron and hole envelope wave function for the QW can be expressed as

$$\Phi_n = \{\Phi_n^j\} \quad (j = 1, 2, \ldots, 8), \quad (6)$$

where

$$\Phi_n^j = \exp[i(k_xx + k_yy)]\sum_m a_{n,m}^j \frac{1}{\sqrt{L}} \exp\left[i\left(k_z + m\frac{2\pi}{L}\right)z\right], \quad (7)$$

and $L = l + d$ is the period of the QW, l and d are the width of the well and barrier layer, respectively. k_x, k_y, and k_z are the wave vectors. n is the index for energy subbands and $a_{n,m}^j$ is the expansion coefficient.

In order to identify the conduction (e), heavy hole (hh), light hole (lh), and spin-orbit split-off (so) band components in the energy states of the QW, we introduced the following probability functions:

$$P_n^e = \sum_{j=1,2}\sum_m a_{n,m}^{j*}a_{n,m}^j,$$

$$P_n^{hh} = \sum_{j=3,6}\sum_m a_{n,m}^{j*}a_{n,m}^j,$$

$$P_n^{lh} = \sum_{j=4,5}\sum_m a_{n,m}^{j*}a_{n,m}^j,$$

$$P_n^{so} = \sum_{j=7,8}\sum_m a_{n,m}^{j*}a_{n,m}^j. \quad (8)$$

By calculating P_n^e, P_n^{hh}, P_n^{lh}, and P_n^{so}, the constituting components of the electron, heavy hole, light hole, and spin-orbit split-off states in the QW state Φ_n can be known. These probability functions are particularly useful in identifying the dominant character in a particular energy state. However, the following sum rule is valid:

$$\sum_i P_n^i = 1, \quad i = e, \text{hh}, \text{lh}, \text{so}. \quad (9)$$

The wave function Φ_n can be classified into two categories, Φ_{n_c} and Φ_{n_v} belongs to conduction band and valence band, respectively, determined according to the position of the energy subband and also the calculated probability functions.

B. Optical transition matrix elements

The squared optical transition matrix elements, which measure the momentum of the transitions between the hole subbands and the electron subbands, are given by[37]

$$Q_i^{n_c n_v} = \frac{2}{m_0}|\langle\Psi_{n_c}|\hat{\boldsymbol{\varepsilon}}\cdot\mathbf{p}_i|\Psi_{n_v}\rangle|^2, \quad i = x, y, z, \quad (10)$$

where $\hat{\boldsymbol{\varepsilon}}$ is the unit vector in the direction of the electric field, $\mathbf{p}_i$ is the momentum operator, and Ψ_{n_c} and Ψ_{n_v} are the real electron and hole wave functions, respectively. The real wave function is the product of the envelope wave functions in Eq. (6) and the Bloch wave functions as listed below,[32]

$$\phi_c(+) = |S\uparrow\rangle,$$

$$\phi_c(-) = |S\downarrow\rangle,$$

$$\phi_v\left(\frac{3}{2}, \frac{3}{2}\right) = -\frac{i}{\sqrt{2}}|(X + iY)\uparrow\rangle,$$

$$\phi_\nu\left(\frac{3}{2},\frac{1}{2}\right) = -\frac{i}{\sqrt{6}}|[(X+iY)\downarrow - 2Z\uparrow]\rangle,$$

$$\phi_\nu\left(\frac{3}{2},-\frac{1}{2}\right) = \frac{i}{\sqrt{6}}|[(X-iY)\uparrow + 2Z\downarrow]\rangle,$$

$$\phi_\nu\left(\frac{3}{2},-\frac{3}{2}\right) = \frac{i}{\sqrt{2}}|(X-iY)\downarrow\rangle,$$

$$\phi_\nu\left(\frac{1}{2},\frac{1}{2}\right) = \frac{i}{\sqrt{3}}|[(X+iY)\downarrow + Z\uparrow]\rangle,$$

$$\phi_\nu\left(\frac{1}{2},-\frac{1}{2}\right) = \frac{i}{\sqrt{3}}|[(X-iY)\uparrow - Z\downarrow]\rangle, \qquad (11)$$

where, $|X\rangle$, $|Y\rangle$, $|Z\rangle$, and $|S\rangle$ are the orbital wave functions of the top of the valence band and the bottom of the conduction band, respectively. $\uparrow$ and $\downarrow$ denote spin-up or spin-down components.

The final expression for squared optical transition matrix elements in the X, Y, and Z direction is given below,[38]

$$Q_{x\uparrow}^{n_c n_\nu} = \frac{2P_0^2}{m_0}\left|\sum_m\left(-\frac{i}{\sqrt{2}}a_{n_\nu,m}^3 + \frac{i}{\sqrt{6}}a_{n_\nu,m}^5 + \frac{i}{\sqrt{3}}a_{n_\nu,m}^8\right)a_{n_c,m}^{1*}\right|^2,$$

$$Q_{x\downarrow}^{n_c n_\nu} = \frac{2P_0^2}{m_0}\left|\sum_m\left(-\frac{i}{\sqrt{6}}a_{n_\nu,m}^4 + \frac{i}{\sqrt{2}}a_{n_\nu,m}^6 + \frac{i}{\sqrt{3}}a_{n_\nu,m}^7\right)a_{n_c,m}^{2*}\right|^2,$$

$$Q_{y\uparrow}^{n_c n_\nu} = \frac{2P_0^2}{m_0}\left|\sum_m\left(\frac{1}{\sqrt{2}}a_{n_\nu,m}^3 + \frac{1}{\sqrt{6}}a_{n_\nu,m}^5 + \frac{1}{\sqrt{3}}a_{n_\nu,m}^8\right)a_{n_c,m}^{1*}\right|^2,$$

$$Q_{y\downarrow}^{n_c n_\nu} = \frac{2P_0^2}{m_0}\left|\sum_m\left(\frac{1}{\sqrt{6}}a_{n_\nu,m}^4 + \frac{1}{\sqrt{2}}a_{n_\nu,m}^6 - \frac{1}{\sqrt{3}}a_{n_\nu,m}^7\right)a_{n_c,m}^{2*}\right|^2,$$

$$Q_{z\uparrow}^{n_c n_\nu} = \frac{2P_0^2}{m_0}\left|\sum_m\left(i\sqrt{\frac{2}{3}}a_{n_\nu,m}^4 + \frac{i}{\sqrt{3}}a_{n_\nu,m}^7\right)a_{n_c,m}^{1*}\right|^2,$$

$$Q_{z\downarrow}^{n_c n_\nu} = \frac{2P_0^2}{m_0}\left|\sum_m\left(i\sqrt{\frac{2}{3}}a_{n_\nu,m}^5 - \frac{i}{\sqrt{3}}a_{n_\nu,m}^8\right)a_{n_c,m}^{2*}\right|^2, \quad (12)$$

and

$$Q_i^{n_c n_\nu} = Q_{i\uparrow}^{n_c n_\nu} + Q_{i\downarrow}^{n_c n_\nu}, \quad i = x,y,z, \qquad (13)$$

where $P_0 = \langle S|p_x|X\rangle = \langle S|p_y|Y\rangle = \langle S|p_z|Z\rangle$. To obtain $Q_{xy}^{n_c n_\nu}$ for the TE model, $Q_x^{n_c n_\nu}$ and $Q_y^{n_c n_\nu}$ are averaged in the calculation. $Q_z^{n_c n_\nu}$ alone indicates the TM model.

Due to the interaction between VB and CB, Φ_{n_c} is not fully a conduction state but will have some components contributed by the valence band and vice versa. Therefore, if more accurate results are required, the contribution from the nonconduction band components in Φ_{n_c} and the nonvalence band components in Φ_{n_ν} must be considered in the derivation of $Q_i^{n_c n_\nu}$. However, the contribution of these nonconventional transitions will be very small as compared to the stronger transitions as depicted in Eq. (12).

C. Carrier density and quasi-Fermi levels

In order to investigate the maximum optical gain obtainable at certain carrier density, the corresponding quasi-Fermi levels must be determined from the integration of the two-dimensional density of states in the quantum well. We have not used the carrier density as calculated for the parabolic energy subbands since the interaction between VB and CB has caused the energy dispersion curves to be nonparabolic. Therefore, a determination of carrier density by numerically integrating over k-space is more appropriate,[39]

$$N = \sum_{n_c}\int\frac{1}{4\pi^2 l}f_c[E_{en_c}(k_x,k_y)]dk_x dk_y,$$

$$P = \sum_{n_\nu}\int\frac{1}{4\pi^2 l}f_\nu[E_{hn_\nu}(k_x,k_y)]dk_x dk_y, \qquad (14)$$

where N and P are the electron and hole density, respectively. E_{en_c} is the electron energy in the conduction subband while E_{hn_ν} is the hole energy (not the electron energy) in the valence subband. f_c and f_ν are the Fermi-Dirac distributions for electrons in the conduction band and holes (not for electron) in the valence band, respectively.[39] They are given by

$$f_c = \frac{1}{1+\exp[(E_{en_c}-E_{f_c})/k_B T]},$$

$$f_\nu = \frac{1}{1+\exp[(E_{hn_\nu}-E_{f_\nu})/k_B T]}, \qquad (15)$$

where E_{f_c} and E_{f_ν} are the electron and hole quasi-Fermi level, respectively, and dependent on carrier density. k_B is the Boltzmann's constant and T is the temperature.

D. Optical gain model

The optical gain spectra are calculated using[40]

$$G(E) = \left[1-\exp\left(\frac{E-\Delta F}{k_B T}\right)\right]\frac{\pi^2 c^2 \hbar^2}{n^2 E^2}R_{sp}(E),$$

$$R_{sp}(E) = \frac{ne^2E}{\pi m_0^2 \varepsilon_0 \hbar^2 c^3} \sum_{n_c} \sum_{n_v} \int \int \frac{Q^{n_c n_v}}{4\pi^2 l} f_c f_v$$

$$\times \frac{1}{\pi} \frac{\hbar/\tau}{(E_{eh} - E)^2 + (\hbar/\tau)^2} dk_x dk_y, \tag{16}$$

where $R_{sp}(E)$ is the spontaneous emission rate, $\Delta F = E_{f_c} - E_{f_v}$ is the quasi-Fermi levels separation and dependent on carrier density, E is the photon energy, e is the electron charge, ε_0 is the free-space dielectric constant, n is the refractive index, c is the speed of light, $Q^{n_c n_v}$ is the squared optical transition matrix element as given in Eqs. (12) and (13), E_{eh} is the transition energy, and τ is the intraband relaxation time. $\tau = 0.1$ ps is used in all our calculations, which are performed at $T = 300$ K, as it is the value widely used for the ideal case of QW simulations.[28,41,42] Although smaller value of τ was proven to better fit the experimental measured spontaneous emission spectrum at room temperature, it will only reduce the peak gain and differential gain linearly.[28] We believe that the fitting of τ depends very much on the quality of samples under study, and our conclusion should not be affected by the value of τ chosen. The radiative current density, which is related to the spontaneous emission spectrum, is given by

$$J_{rad} = el \int R_{sp}(E) dE. \tag{17}$$

This is different from injection current density, which includes not only J_{rad}, but also contribution from monomolecular, Auger recombinations, etc.

E. 10-band model

In order to take into account the influence of the band structure by the nitrogen-induced level, E_N, a 10-band $\mathbf{k} \cdot \mathbf{p}$ model was proposed which add two more spin-degenerated states to the 8-band Hamiltonian in Eq. (1) through the following matrix:[28,43]

$$H_k + H_s = \begin{bmatrix} N & 0 & V_{NC}\sqrt{y} & 0 \\ 0 & N & 0 & V_{NC}\sqrt{y} \\ V_{NC}\sqrt{y} & 0 & C & 0 \\ 0 & V_{NC}\sqrt{y} & 0 & C \end{bmatrix}, \tag{18}$$

where

$$N = E_N + \varepsilon_2(z). \tag{19}$$

We have shifted E_N by the amount of energy caused by the shear strain, $\varepsilon_2(z)$, since the origin of our calculation is at the middle of the heavy-hole and light-hole band edge after splitting. For compressive strain, the heavy-hole band edge is taken as the valence band maximum. We have neglected the interaction between E_N and the valence subbands,[44] which is consistent with assumption of the band anticrossing model that the influence of E_N on valance band energy is minimal and negligible.[21] The two new additional Bloch wave functions are[28]

TABLE I. Parameters for binary compounds used in the band structure calculation (Ref. 33).

Quantity	GaAs	InAs	GaN	InN
a_0 (Å)	5.6533	6.0583	4.50	4.98
Δ (eV)	0.341	0.390	0.017	0.006
a_c (eV)	−7.17	−5.08	−2.20	−1.85
a_v (eV)	1.16	1.00	5.20	1.50
b (eV)	−2.0	−1.8	−2.2	−1.2
c_{11} (GPa)	122.1	83.29	293.0	187.0
c_{12} (GPa)	56.6	45.26	159.0	125.0
γ_1^L	6.98	20.00	2.67	3.72
γ_2^L	2.06	8.50	0.75	1.26
γ_3^L	2.93	9.20	1.10	1.63
E_P (eV)	28.8	21.5	25.0	25.0

$$\phi_N(+) = |S_N \uparrow\rangle,$$

$$\phi_N(-) = |S_N \downarrow\rangle. \tag{20}$$

The significance of E_N and V_{NC} will be explained in a later section.

F. Band parameters

The band parameters of the parental binary compounds used in our calculations is taken from Ref. 33 and listed in Table I. The parameters for $In_xGa_{1-x}As$ and $In_xGa_{1-x}As_{1-y}N_y$ are interpolated as follows:

$$P(In_xGa_{1-x}As) = (1-x)P(GaAs) + xP(InAs),$$

$$P(In_xGa_{1-x}As_{1-y}N_y) = (1-x)(1-y)P(GaAs) + x(1-y)$$
$$\times P(InAs) + (1-x)yP(GaN)$$
$$+ xyP(InN). \tag{21}$$

However, for band gap energy and electron effective mass of $In_xGa_{1-x}As$, we have included the bowing parameters as recommended,[33]

$$E_G(In_xGa_{1-x}As) = (1-x)E_G(GaAs) + xE_G(InAs)$$
$$- 0.477x(1-x),$$

$$m_e^*(In_xGa_{1-x}As) = (1-x)m_e^*(GaAs) + xm_e^*(InAs)$$
$$- 0.0091x(1-x). \tag{22}$$

The phenomenological relationship that predicts the heavy m_e^* of $In_xGa_{1-x}As_{1-y}N_y$ is given by[31]

$$m_e^*(In_xGa_{1-x}As_{1-y}N_y) = m_e^*(In_xGa_{1-x}As) + 18.1667m_0$$
$$\times \Delta e(x,y), \tag{23}$$

where $\Delta e(x,y)$ is the difference of strain between $In_xGa_{1-x}As_{1-y}N_y$ and $In_xGa_{1-x}As$. While the m_e^* of $In_xGa_{1-x}As_{1-y}N_y$ as predicted by the BAC model is given by[22,45]

$$m_e^*(\text{In}_x\text{Ga}_{1-x}\text{As}_{1-y}\text{N}_y) = 2m_e^*(\text{In}_x\text{Ga}_{1-x}\text{As}) \bigg/ \left(1 - \frac{E_C - E_N}{\sqrt{(E_C - E_N)^2 + 4V_{NC}^2 y}}\right). \tag{24}$$

G. Nitrogen-related band parameters

Two of the most important parameters in BAC model are E_N and V_{NC}, which characterize the position of the nitrogen-induced energy level with respect to valence band maximum (VBM) and the matrix element measuring the strength of interaction between E_C and E_N, respectively. The E_- in the BAC model is taken to be the fundamental band gap energy (E_G) for $\text{In}_x\text{Ga}_{1-x}\text{As}_{1-y}\text{N}_y$,

$$E_- = \frac{1}{2}[(E_N + E_C) - \sqrt{(E_N - E_C)^2 + 4V_{NC}^2 y}], \tag{25}$$

where y is the nitrogen composition in $\text{In}_x\text{Ga}_{1-x}\text{As}_{1-y}\text{N}_y$.

There are two sets of E_N and V_{NC} available. The first set has been proven to agree very well with experimental E_G in $\text{GaAs}_{1-y}\text{N}_y$,[22,23]

$$E_N = 1.65(1 - x) + 1.44x - 0.38x(1 - x),$$

$$V_{NC} = 2.7(1 - x) + 2.0x - 3.5x(1 - x). \tag{26}$$

However, the second set is able to yield better agreement with $\text{In}_x\text{Ga}_{1-x}\text{As}_{1-y}\text{N}_y$ in the range where indium is 30% to 40%, after taken into consideration the statistical local N environment,[24]

$$E_N = 1.65 + 0.25x - 0.56x,$$

$$V_{NC} = 2.4(1 - x) + 1.75x. \tag{27}$$

The bulk band gap energy and m_e^* [using Eq. (24)] predicted by these two sets of parameters is compared in Figs. 1(a) and 1(b), respectively. In Fig. 1(b), we observe that m_e^* calculated by BAC model depends not only on nitrogen composition but also indium composition. As indium composition increases, the enhancement of m_e^* by the addition of nitrogen atom is reduced significantly. We have also plotted the m_e^* given by the phenomenological relationship in Eq. (23) in Fig. 1(b) for comparison and observed that it generally predicted heavier m_e^* than the BAC model. A comparison between the calculations of 10-band $\mathbf{k} \cdot \mathbf{p}$ model with the experimental values of measured photoluminescence wavelengths has been performed and will be presented in next section.

H. Other considerations

Due to the various $\mathbf{k} \cdot \mathbf{p}$ models presented in the literatures, we have also included three other $\mathbf{k} \cdot \mathbf{p}$ models without VB and CB interaction, namely, 6+2-band, 6+2-band with heavy m_e^* as predicted by Eq. (23), and the 6+4-band. These models can be obtained from the same Hamiltonians for 8-band and 10-band models by setting the matrix elements (P) to zero, which signifies no interaction between CB and

VB. The Hamiltonians are then decoupled into the 6-band model for valence band and 2-band for 8-band model, or 4-band for 10-band model in the conduction band. Under such condition, the modified Luttinger parameters are identical to the original Luttinger parameters. The details for the $\mathbf{k} \cdot \mathbf{p}$ models used in the report are summarized in Table II.

The strained conduction band offset (Q_C) for $\text{In}_x\text{Ga}_{1-x}\text{As}/\text{GaAs}$ QW is taken to be 0.63 and 0.70 at indium composition of 15% and 35%, respectively. These values were derived from the best-fit curve to the available experimental data. Q_C for $\text{In}_x\text{Ga}_{1-x}\text{As}_{1-y}\text{N}_y/\text{GaAs}$ QW is calculated by assuming that the unstrained valence band offset for both $\text{In}_x\text{Ga}_{1-x}\text{As}_{1-y}\text{N}_y/\text{GaAs}$ and $\text{In}_x\text{Ga}_{1-x}\text{As}/\text{GaAs}$ to be identical. The band gap energy for $\text{In}_x\text{Ga}_{1-x}\text{As}_{1-y}\text{N}_y$ is then lowered from that of $\text{In}_x\text{Ga}_{1-x}\text{As}$ according to the BAC model to determine Q_C for $\text{In}_x\text{Ga}_{1-x}\text{As}_{1-y}\text{N}_y/\text{GaAs}$ QW.

III. RESULTS AND DISCUSSIONS

The results were calculated using an $\text{In}_x\text{Ga}_{1-x}\text{As}_{1-y}\text{N}_y/\text{GaAs}$ QW, with well width (l) of 7 nm and barrier width (d) of 20 nm at $T = 300$ K. The main focus of the calculation is in the range of $x = 35\%$ and $y = 0$ to 4%. These should cover the range of composition of reported laser structures emitting at 1.3 and near 1.55 μm.[2–18] We have compared our calculation of band structure with a strained 3 nm $\text{InAs}/\text{In}_{0.4}\text{Ga}_{0.6}\text{Sb}$ superlattice[46] and an unstrained 5 nm $\text{GaAs}/\text{Al}_{0.3}\text{Ga}_{0.7}\text{As}$ quantum well.[47] Our results agree very well with the published literatures.

In order to verify our theoretical model, we have performed some calculations based on the 10-band $\mathbf{k} \cdot \mathbf{p}$ model and compared them with the emission wavelengths reported
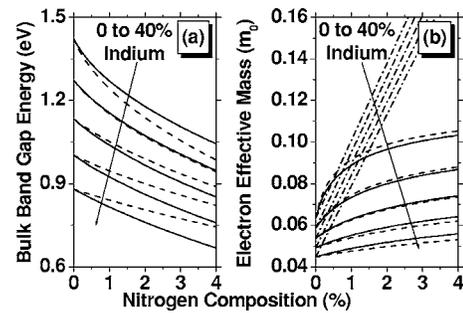
FIG. 1. Dependence of (a) bulk band gap energy and (b) electron effective mass (m_e^*) of $\text{In}_x\text{Ga}_{1-x}\text{As}_{1-y}\text{N}_y$ material on indium and nitrogen composition. In (a), the bulk band gap energy was calculated using Eq. (25). In (b), m_e^* (except the dotted-dashed lines) is calculated using Eq. (24). Solid lines and dashed lines in both figures are the results calculated using the sets of E_N and V_{NC} from Eq. (27) and Eq. (26), respectively. Dotted-dashed lines in (b) are for m_e^* calculated using phenomenological relationship from Eq. (23).

TABLE II. Details of $\mathbf{k} \cdot \mathbf{p}$ models used in this paper.

Model	CB and VB interaction	Presence of E_N	Electron effective mass	Valence band parameters
10-band	Yes	Yes	InGaAs's	InGaAs's
8-band	Yes	No	InGaAsN's by BAC model	InGaAsN's
6+2-band	No	No	InGaAsN's by BAC model	InGaAsN's
6+2-band with heavy m_e^*	No	No	InGaAsN's by phenomenological relationship	InGaAsN's
6+4-band	No	Yes	InGaAs's	InGaAsN's

in the literatures. The results are presented in Table III. As can be seen, the transition energies (E_{eh}) predicted by the 10-band model agrees reasonably well with the experimental values. We expect a better agreement if many-body effects, which include band gap renormalization and Coulomb enhancement, are being considered in the optical gain calculation. The typical shift caused by band gap renormalization in

$In_xGa_{1-x}As/GaAs$ QW has been shown to be around 40 to 50 meV.[48]

We have calculated the energy dispersion curves along [100] and [110] crystal directions for conduction and valence subbands for $In_xGa_{1-x}As_{0.98}N_{0.02}/GaAs$ QW using the five models described in Table II. The results for nitrogen composition of 2%, and indium composition of 35% and 15% are

TABLE III. Comparison of theoretical transition energies of $In_xGa_{1-x}As_{1-y}N_y/GaAs$ by 10-band $\mathbf{k} \cdot \mathbf{p}$ model with experimental values.

Well layer composition		Well width (nm)	Theoretical values (1) (eV)	Experimental value (2) (eV)	Difference (1)–(2) (meV)
Indium (%)	Nitrogen (%)				
36	1.9	6.8	0.946	0.954[a]	−8
32	1.5	7.0	1.002	0.943[b]	59
36	1.6	6.0	0.978	0.942[c]	36
32	1.0	9.0	1.020	0.954[d]	66
37	0.5	7.7	1.028	0.961[e]	67
32	0.9	10.0	1.025	0.969[f]	56
40	0.5	6.0	1.020	0.958[g]	62
35	1.5	6.0	0.993	0.959[h]	34
35	1.8	6.5	0.964	0.965[i]	−1
35.5	3.6	9.2	0.828	0.795[j]	33
38	5.0	7.6	0.759	0.832[k]	−73
38	5.3	8.2	0.739	0.800[l]	−61
38	5.0	7.6	0.759	0.817[m]	−58
34	5.3	6.5	0.786	0.795[n]	−9
38	3.3	8.0	0.836	0.785[o]	51
20.4	5.5	7.2	0.852	0.800[p]	52
26	3.0	9.0	0.932	0.821[q]	111

[a]Reference 2.
[b]Reference 3.
[c]Reference 4.
[d]Reference 5.
[e]Reference 6.
[f]Reference 7.
[g]Reference 8.
[h]Reference 9.
[i]Reference 10.

[j]Reference 11.
[k]Reference 12.
[l]Reference 13.
[m]Reference 14.
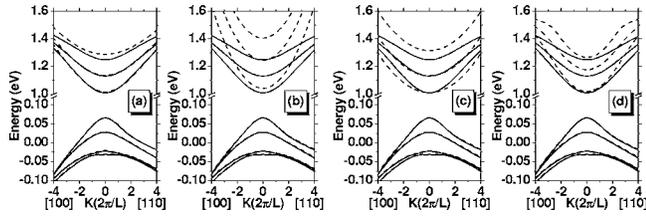[n]Reference 15.
[o]Reference 16.
[p]Reference 17.
[q]Reference 18.

FIG. 2. Energy dispersion curves for conduction and valence subbands along [100] and [110] crystal directions for a 7 nm $In_{0.35}Ga_{0.65}As_{0.98}N_{0.02}$/GaAs quantum well. Solid lines in every graph are the results calculated by 10-band $\mathbf{k \cdot p}$ model. Comparison is made with dashed lines in (a) 8-band, (b) 6+2-band, (c) 6+2-band with heavy m_e^*, and (d) 6+4-band model.

shown in Figs. 2 and 3, respectively. The solid lines are the results calculated by 10-band model, and are being compared with the remaining four models. As can be observed from Fig. 2(a), the 8-band's results agree very well with that of 10-band at high indium composition (35%). This confirmed our initial assumption that by using the electron effective mass (m_e^*) calculated by the BAC model in the 8-band model, we should be able to obtain identical conduction band structure with the 10-band model, at least for the first two conduction subbands. However, at low indium composition (15%), the agreement deteriorates; see Fig. 3(a). In this case, the second and third conduction subbands are very close to one another. This is due to the fact that in the 10-band model, the conduction band structures of $In_{0.15}Ga_{0.85}As$/GaAs calculated by the 8-band model will interact with the two nitrogen-related resonant states. Moreover, at low indium, the conduction band barrier height in the $In_{0.15}Ga_{0.85}As$/GaAs QW is very low, this causes that only first conduction subband is confined in the well, and the subsequent two higher energy subbands are unbound. After interacting with the E_N, the second and third energy subbands remain very near to one another as in 10-band's results. However, in the 8-band model, the conduction band barrier height used is that of $In_{0.15}Ga_{0.85}As_{0.98}N_{0.02}$/GaAs QW, which is larger than that of $In_{0.15}Ga_{0.85}As$/GaAs QW. In addition, m_e^* being used in the 8-band model is that of $In_{0.15}Ga_{0.85}As_{0.98}N_{0.02}$, which is heavier than that of $In_{0.15}Ga_{0.85}As$. This explains why the first three energy subbands in the 8-band model are still confined in the potential well.
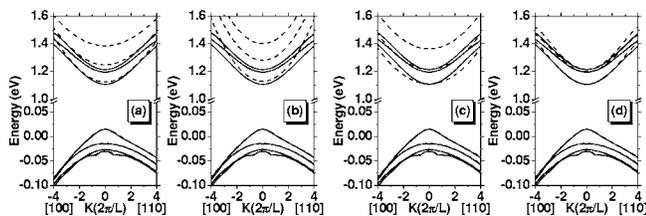

FIG. 3. Energy dispersion curves for conduction and valence subbands along [100] and [110] crystal directions for a 7 nm $In_{0.15}Ga_{0.85}As_{0.98}N_{0.02}$/GaAs quantum well. Solid lines in every graph are the results calculated by 10-band $\mathbf{k \cdot p}$ model. Comparison is made with dashed lines in (a) 8-band, (b) 6+2-band, (c) 6+2-band with heavy m_e^*, and (d) 6+4-band model.
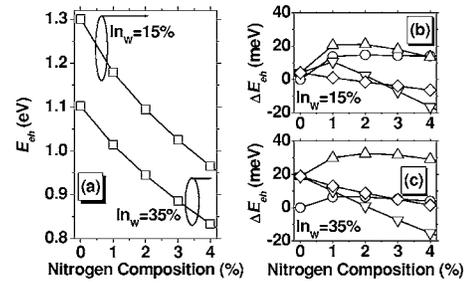

FIG. 4. Dependence of transition energy E_{eh} for a 7 nm $In_xGa_{1-x}As_{1-y}N_y$/GaAs quantum well on nitrogen composition for In_w=15% and 35%. (a) Results of the 10-band $\mathbf{k \cdot p}$ model. (b) and (c) are the deviations of transition energy (ΔE_{eh}) for other models from that of the 10-band calculation for In_w=15% and 35%, respectively. (□) denotes results of 10-band, (○) denotes results of 8-band, (△) denotes results of 6+2-band, (∇) denotes results of 6+2-band with heavy m_e^*, and (◇) denotes results of 6+4-band.

When comparing the results calculated by the 6+2-band with those of 10-band model in Figs. 2(b) and 3(b), we can observe that with the interaction of VB and CB taken into account, and further flattening of the band structure by E_N, the 10-band results is highly nonparabolic. Another effect of the VB and CB interaction as in the 8-band model is to bring down the second conduction subband and this reduces the energy separation between the first two conduction subbands. This will definitely increase the density of states near the conduction band edge, and may have detrimental effect on the differential gain. However, when the heavy m_e^* predicted by the phenomenological relationship was being used in the 6+2-band model, as being shown in Fig. 2(c), the energy separation is the same as that of the 10-band model despite the VB and CB interaction was neglected in the model. Upon closer examination, the first conduction subband is flatter than that of the 10-band, which implies that if the band structure calculated by the 10-band is the correct one, then the real bulk m_e^* of the $In_xGa_{1-x}As_{1-y}N_y$ material may not be that heavy as predicted by the phenomenological relationship in Eq. (23).

From the comparison of the energy dispersion curves calculated by 6+4-band and 10-band models, see Fig. 2(d) and 3(d), we can observe that agreement between the calculated transition energy is reasonably good although the VB and CB interaction was neglected in the former model. This has something to do with the strain band parameters, such as a_c, a_v, and b, used in the calculation. As can be observed from Table II, the strain band parameters for 6+4-band and 10-band models are that of $In_xGa_{1-x}As_{1-y}N_y$ and $In_xGa_{1-x}As$, respectively. While the VB and CB interaction was not considered, the calculated E_{eh} should be higher for the 6+4-band's results, as in the comparison between 6+2-band and 8-band models. However, the strained band gap energy calculated for the 6+4-band model is actually lower than that calculated for the 10-band model and thus compensating the increase due to the lack of VB and CB interaction. For a clearer view of these results, we have plotted the deviation of the calculated results for other models when compared to the 10-band model. Figures 4 and 5 show the consolidated results for E_{eh} and $e2-e1$, respectively.
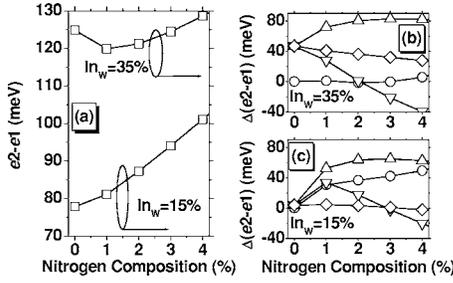
FIG. 5. Dependence of energy separation between the first two conduction subbands ($e2-e1$) for a 7 nm $In_xGa_{1-x}As_{1-y}N_y$/GaAs quantum well on nitrogen composition for $In_w=15\%$ and 35%. (a) Results of the 10-band $\mathbf{k} \cdot \mathbf{p}$ model. (b) and (c) are the deviations of $e2-e1[\Delta(e2-e1)]$ for other models from that of the 10-band calculation for $In_w=35\%$ and 15%, respectively. Same legend from Fig. 4 applies.

FIG. 6. Dependence of (a) transparency carrier density (N_{tr}) and (b) transparency radiative current density ($J_{rad(tr)}$) for a 7 nm $In_{0.35}Ga_{0.65}As_{1-y}N_y$/GaAs quantum well on nitrogen composition for various models considered here. Same legend from Fig. 4 applies.

As pointed out in the last paragraph, at indium composition equal to 35%, E_{eh} predicted by the 6+2-band with BAC's m_e^* is consistently about 20 meV higher than that predicted by the 8-band due to the lack of interaction between VB and CB, although both models used the same set of band parameters for the calculation. This confirmed that VB and CB interaction must be included in the simulation of $In_xGa_{1-x}As_{1-y}N_y$ QW for a more realistic representation of the band structure, especially when the band gap energy is lower. However, in the case of 6+4-band and 10-band model, their band parameters are not the same, except for m_e^*. This different treatment is due to the fact that we would like to replicate some of the results as presented in Ref. 25 for the 6+4-band here and therefore we must be faithful to the method they used.

As can be observed from Figs. 2 and 3, the interaction between VB and CB and the inclusion of the BAC model in the conduction band has very little effect on the energy dispersion curves of valence subbands, even though some of the models used $In_xGa_{1-x}As_{1-y}N_y$'s band parameters and others used $In_xGa_{1-x}As$'s band parameters. This is due to the fact that although $In_xGa_{1-x}As_{1-y}N_y$'s band parameters are dependent on the nitrogen composition, which is less than 5% in our calculation, the differences between the two sets of band parameters are not great enough to effect any significant modification to the band structure in the valence band.

In summary, at high indium composition, both E_{eh} and $e2-e1$ predicted by the 8-band model are the closest to that calculated by the 10-band model, which implies that 8-band model is a good enough alternative for the 10-band model from the aspect of band structure calculation in the high indium range (35%). However, at low indium range (15%), E_{eh} and $e2-e1$ calculated by the 6+4-band is the closest thus far to the results predicted by the 10-band. Nevertheless, we are aware that the validity of the very closely located second and third conduction subbands cannot be established without any further investigation by accurate absorption measurements.

After comparing the band structure calculated by different models, we are interested to know their impact on the prediction of optical properties at transparency condition since that was the focus of most studies. We have determined the quasi-Fermi energy levels (E_{f_c} and E_{f_v}) for the preselected
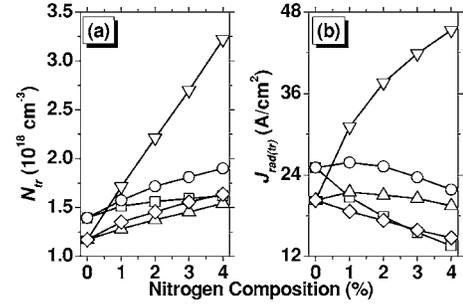
interval of carrier density, because they will be the input to the optical gain calculation instead of the carrier density. Subsequently, the dependence of material optical gain of $In_xGa_{1-x}As_{1-y}N_y$/GaAs on carrier density and radiative current density is being determined. We are interested to know the point when the optical gain transits from the negative (loss) to the positive (amplification) region. The results are being plotted in Fig. 6. Figures 6(a) and 6(b) show the carrier density (N_{tr}) and radiative current density ($J_{rad(tr)}$) at transparency. As anticipated, since the valence subbands for all models are almost similar, even for the 10-band model which uses InGaAs's parameters or the 8-band and 6-band model which uses InGaAsN's band parameters, N_{tr} can be concluded to be mainly dependent on the m_e^* in the conduction band structure and VB and CB interaction. The relationship is consistent with the m_e^* plotted in Fig. 1(b). The increase in N_{tr} from 0% to 2% of nitrogen is greater than that from 2% to 4% of nitrogen and can be easily understood since the increase in m_e^* is greater for 0% to 2% of nitrogen. Of greater importance is that the 6+2-band model with heavy m_e^* predicts N_{tr} which is almost double that of other models. Therefore, the value of m_e^* does affect N_{tr} very much. In Fig. 6(b), however, only the 6+2-band model with heavy m_e^* is showing a monotonous increase in $J_{rad(tr)}$. These may at first seem to be contrary to the results calculated by the 10-band model, which observed weak dependence of $J_{rad(tr)}$ on nitrogen composition.[41] Upon closer comparison, we observed that in Ref. 41, both indium and nitrogen composition were varied while maintaining the emission wavelength at 1.3 μm, as opposed to ours, which only varied nitrogen composition and results in different emission wavelengths. Therefore, the weak dependence observed is partly due to the decrease in indium composition and compressive strain that could result in higher $J_{rad(tr)}$ in the QWs. The reduction in $J_{rad(tr)}$ with increasing nitrogen composition, in our results, can be attributed to two factors, (1) the reduction in transition energy which directly affects the radiation current density at transparency [according to Eqs. (16) and (17)], (2) the stronger interaction between the conduction subbands with either the nitrogen resonant energy level (for the 10-band and the 6+4-band models) or valence subbands (for 10-band, 8-band) thus causing lower strength of $Q_{xy}^{n_c n_v}$ at $k=0$. Since in the
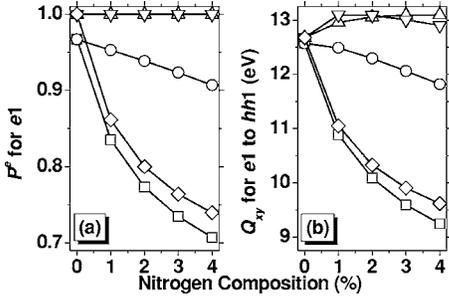
FIG. 7. Dependence of (b) $P_{n_c}^e$ for first conduction subband, $e1$ and (b) TE-mode squared transition matrix elements for $e1$ to $hh1$ transition for various models on nitrogen composition at $k=0$ in a $In_{0.35}Ga_{0.65}As_{1-y}N_y/GaAs$ quantum well. Same legend from Fig. 4 applies.

10-band model, $J_{rad(tr)}$ is under the influence of the two factors mentioned above, its reduction with nitrogen composition is the greatest as can be observed in Fig. 6(b). However, in the case of the 6+2-band model with heavy m_e^*, the heavier electron mass not only caused the quantum well to achieve transparency at higher carrier density, but it also produced a greater J_{rad} with its much flatter conduction band structure and better overlapping of Φ_{n_c} and Φ_{n_v}, and thus higher $Q_{xy}^{n_c n_v}$ at $k \neq 0$. The probability function $P_{n_c}^e$ for the first conduction subband is given in Fig. 7(a) to show the degree of band intermixing mentioned above. Figure 7(b) shows the $Q_{xy}^{n_c n_v}$ at $k=0$, which clearly shows the declining of momentum for optical transition with increasing nitrogen composition. Our $J_{rad(tr)}$ is comparatively lower than other published values. However, recent experimental determinations of $J_{rad(tr)}$ for $In_{0.4}Ga_{0.6}As_{0.995}N_{0.005}/GaAs/GaAs_{0.85}P_{0.15}$ and $In_{0.4}Ga_{0.6}As/GaAs/GaAs_{0.85}P_{0.15}$ single QWs with well width of 6 nm agree with our calculation results,[49] especially with the prediction of lower $J_{rad(tr)}$ with increasing nitrogen composition by the 10-band and 6+4-band models. Their measured $J_{rad(tr)}$ of about 15 ± 2 A/cm^2 and 19 ± 2A/cm^2, for structure with and without nitrogen, have demonstrated the ability of achieving low current density at both transparency and threshold for InGaAsN-based QWs. It also reveals the possibility of achieving a lower $J_{rad(tr)}$ with InGaAsN active layer than with InGaAs layer of the same indium composition.

It now becomes obvious that the prediction of m_e^* for $In_xGa_{1-x}As_{1-y}N_y$ at indium of around 30% to 40% by the phenomenological relationship or simple BAC model [see Fig. 1(b)] does affect the results greatly, especially in the prediction of N_{tr} and $J_{rad(tr)}$. While the measurements have shown that $GaAs_{1-y}N_y$ and lattice matched $In_xGa_{1-x}As_{1-y}N_y$ layers exhibit large enhancement of m_e^*, the measurement of m_e^* in high indium range involves great difficulties since the growth of thick free standing epilayer for accurate measurements, typically 1 to 3 μm thick,[50,51] is inherently challenging. Currently, the only direct determination of m_e^* for $In_xGa_{1-x}As_{1-y}N_y$ was reported in Ref. 50. However, the m_e^* of $0.4m_0$ for $In_{0.08}Ga_{0.92}As_{0.967}N_{0.033}$ was determined from reflectivity spectra, at an electron concentration of 6×10^{19} cm^{-3}, when the Fermi level is high up in the con-

duction band, where the band structure is flattened due to the presence of nitrogen resonant level according to the BAC model. The same author admits that reflectivity measurements are unable to determine accurately m_e^* at the bottom of the conduction band.[45] Other measurements are being performed on $GaAs_{1-y}N_y$ material.[51–53] Using optically detected cyclotron resonance (ODCR) technique, m_e^* of $0.12m_0$ and $0.19m_0$ were obtained for $GaAs_{0.988}N_{0.012}/GaAs$ and $GaAs_{0.98}N_{0.02}/GaAs$ multiple quantum wells, respectively.[52,53] The larger measured m_e^* in $GaAs_{1-y}N_y$ than that predicted by the BAC model has been attributed to the possible strong interaction between the CB edge of the host matrix and the nitrogen cluster states resulted in hybridization that can further increase m_e^*.[54,55] Note, the measurements performed using the method of four coefficients on $GaAs_{1-y}N_y$ thin film yields different results, with m_e^* decreases from 0.084 to 0.029 as nitrogen composition increases from 0 to 0.4%.[51] Although there is another independent report that gives the same finding, by inferring m_e^* for $GaAs_{1-y}N_y$ of $0.55m_0$ for 1% of nitrogen and $0.15m_0$ for 4% nitrogen from their own measurements,[56] these results are controversial because of their fitting by parabolic conduction band using a simple quantum well model.[45] The widely accepted understanding is still that m_e^* will increase with nitrogen composition in $GaAs_{1-y}N_y$ material.[55] However, many reports [including Eq. (23)] have tried to assume the large enhancement of m_e^* observed in $GaAs_{1-y}N_y$ will not be affected by the addition of indium into $In_xGa_{1-x}As_{1-y}N_y$ layer. The initial samples for $In_xGa_{1-x}As_{1-y}N_y/GaAs$ QWs were showing high threshold current density of above 1 kA/cm^2 when more nitrogen is being added into the well layer,[3,5] especially for those that are emitting near 1.55 μm, thus lending support to the view that m_e^* for $In_xGa_{1-x}As_{1-y}N_y$ is heavy according to the phenomenological relationship, especially according to the results shown in Fig. 6(b) for the 6+2-band model with heavy m_e^*. However, it has been shown recently that the major part that contributed to the large threshold is due to the nonradiative monomolecular recombination that can be reduced using better processing technique during the fabrication of the laser.[57] Therefore, we believe that the lower enhancement of m_e^* for $In_xGa_{1-x}As_{1-y}N_y$ as predicted by the BAC model is more reasonable since it has been shown to agree very well with the measured radiative current density (through 10-band $\mathbf{k} \cdot \mathbf{p}$ model) (Ref. 57) and the assignment of energy levels in photomodulated reflectance measurements.[43] In summary, according to the BAC model, with statistical local N environment taken into consideration as in Eq. (27), we believe that the enhancement of m_e^* in $In_xGa_{1-x}As_{1-y}N_y$ will be weakened as more indium is added into the well layer since the downward shift of E_C with respect to valence band maximum is greater than that of E_N, resulting in reduced interaction between E_C and E_N.

Another important property for the design of semiconductor laser is the differential gain, which determines the modulation speed for the device. We have plotted the maximum obtainable TE-mode differential gain with respect to carrier density (dG/dN) and radiative current density (dG/dJ_{rad}) in Fig. 8(a) and 8(b), respectively. Our dG/dN of 0.7×10^{-15} cm^2 for $In_{0.35}Ga_{0.65}As/GaAs$ QW is
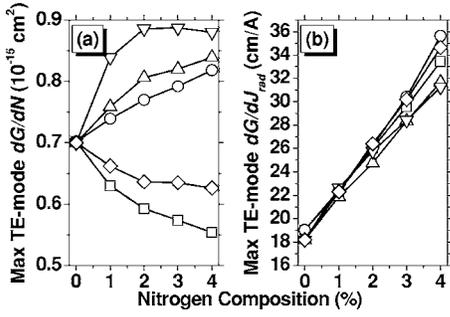
FIG. 8. Dependence of maximum differential gain (a) dG/dN and (b) dG/dJ_{rad} for a 7 nm $In_{0.35}Ga_{0.65}As_{1-y}N_y$/GaAs quantum well on nitrogen composition for various models considered here. Same legend from Fig. 4 applies.

comparable to the values published in other literatures. In Ref. 42, dG/dN between 0.8×10^{-15} and 1.4×10^{-15} cm^2 were obtained for $In_xGa_{1-x}As$/GaAs QWs emitting at 0.98 μm with indium varied from 15% to 30%. At a well width of 8.5 nm, dG/dN of 0.7×10^{-15} cm^2 was obtained for $In_{0.52}Ga_{0.48}As$/$In_{0.86}Ga_{0.14}As_{0.3}P_{0.7}$, although without strain.[58] However, higher dG/dN were also reported, with about 2×10^{-15} cm^2 for 8 nm $In_{0.35}Ga_{0.65}As$/$Al_{0.20}Ga_{0.80}As$ QW,[59] and 2.5×10^{-15} cm^2 for 7 nm $In_{0.55}Ga_{0.45}As$/GaAs.[28,41] We believe the higher dG/dN were obtained when smaller strained conduction band offset ratio (Q_C) were used. In Refs. 28, 41, and 59, Q_C of about 0.62 was used. Reference 42 used Q_C of 0.65, while Q_C of 0.70 was used in our calculations. Although the corresponding increase in the valence band discontinuity has very little effect on the heavy-hole energy states, the light-hole energy will be moved further towards the barrier's valence band maximum. Consequently, the heavy-hole and light-hole band mixing that is detrimental to the TE-mode transition is reduced and the valence band density of states will be reduced too, causing larger ΔF as in Eq. (16). These will definitely result in higher TE-mode dG/dN in the calculations of gain characteristics.

One of the important observations is that dG/dN for the 10-band model is decreasing with increase in nitrogen composition while the opposite was observed in the prediction by the 8-band model. The reduction of dG/dN in 10-band model was also observed in Ref. 41. The presence of E_N actually reduces the magnitude of $P^e_{n_c}$ [as shown in Fig. 7(a)] with increasing nitrogen composition due to stronger interaction between nitrogen and conduction bands. Since we are taking the orbital wave function $|S_N\rangle$ for the nitrogen-induced level to be different from $|S\rangle$ for conduction band and it is not involved in the radiative transition, the decrease in $P^e_{n_c}$ is detrimental to dG/dN. Looking at Fig. 8(a) again, dG/dN actually decreases with VB and CB interaction. This is due to the reduction in energy separation between $e1$ and $e2$ in the conduction band, which results in lowering of separation between quasi-Fermi levels, ΔF, as the density of states increases near the bottom of the conduction band. However, the 6+2-band with heavy m_e^* yield the highest dG/dN even when its N_{tr} is the highest among that predicted by other models. As mentioned above, with larger m_e^*, the overlapping

between Φ_{n_c} and Φ_{n_v} is improved, which increases optical gain and radiative current density through the increase in $Q^{n_cn_v}_{xy}$. Therefore, the dG/dJ_{rad} is almost the same as calculated by other models. The monotonous increase in dG/dJ_{rad} with nitrogen composition in Fig. 8(b) is related to the lowering of transition energy by the addition of nitrogen atoms. The lower E_{eh} restricted the increment in J_{rad} while the increase in gain continues to outpace that of J_{rad}.

We now know that the choice of orbital function for the nitrogen resonant level affects the optical properties greatly, especially for dG/dN. The reduction in optical transition matrix elements when considering E_N in the $\mathbf{k \cdot p}$ model is first reported in Ref. 27, in which the InGaAsN/GaAs QW was compared with a nitrogen-free InGaAs/GaAs with the transition energy artificially lowered. The optical gain obtained by the former is smaller than the latter. The reason given was due to the increase in m_e^* caused by the band anticrossing. Other reports while presenting the same finding with decrease in TE-mode optical gain with increase in nitrogen composition offers little detailed explanation.[60] However, as being discussed earlier, greater m_e^* actually resulted in better overlapping of wave functions from conduction and valence subband and higher dG/dN. The weakening of optical transition matrix elements even at $k=0$ is actually due to the stronger interaction between nitrogen and conduction band. The finding by pseudopotential supercell calculation on $GaAs_{1-y}N_y$ reveals that interband transition elements is strongly dependent on composition, which is large for small nitrogen composition and very small for large nitrogen composition.[61] Therefore, our assumption that the nitrogen-like states are not contributing to the radiative transition is appropriate. Consequently, the intermixing of E_C and E_N results in the reduction of $Q^{n_cn_v}_{xy}$ as illustrated in the 10-band and 6+4-band models and predicted degrading of dG/dN with the addition of a nitrogen atom.

IV. CONCLUSIONS

In conclusion, we have performed calculation of energy dispersion curves and optical emission spectra with different formalisms of $\mathbf{k \cdot p}$ method. We have found that at high indium composition (35%), both E_{eh} and $e2-e1$ predicted by the 8-band model are the closest to that calculated by the 10-band model, which implies that the 8-band model is a good enough alternative for the 10-band model from the aspect of band structure calculation in the high indium range; at low indium range (15%), the E_{eh} and $e2-e1$ calculated by 6+4-band model is the closest to the results predicted by the 10-band model. The m_e^* of $In_xGa_{1-x}As_{1-y}N_y$ as predicted by the BAC model is more reasonable and the enhancement caused by the addition of nitrogen atom is weakened as the indium composition increased. We have discovered that whenever the interaction between VB and CB is neglected, the differential gain (dG/dN) obtained is higher and the N_{tr} is lower, than the values obtained by those models which considered VB and CB interaction in the calculations due to the effect of band mixing. In addition, the higher m_e^* predicted by the phenomenological relationship, when used in

the 6-band model, monotonously predicted higher dG/dN and also $J_{rad(tr)}$ when the nitrogen content increases. The degrading of dG/dN and even optical gain obtainable at fixed carrier density calculated by the inclusion of the BAC model into the 10-band $\mathbf{k} \cdot \mathbf{p}$ model is due to the fact that more components of the conduction band states are intermixed with the nonradiative nitrogenlike states. The difference in the prediction of dG/dN by the 8-band (predicted an increase) and the 10-band model (predicted a reduction) in this paper will prompt for a more detailed investigation of the use of the various simplified $\mathbf{k} \cdot \mathbf{p}$ formalisms to predict the various device performances.

[1] M. Kondow, K. Uomi, A. Niwa, T. Kitatani, S. Watahiki, and Y. Yazawa, Jpn. J. Appl. Phys., Part 1 **35**, 1273 (1996).

[2] D. A. Livshits, A. Yu. Egorov, and H. Riechert, Electron. Lett. **36**, 1381 (2000).

[3] W. Ha, V. Gambin, M. Wistey, S. Bank, S. Kim, and J. S. Harris, Jr., IEEE Photonics Technol. Lett. **14**, 591 (2002).

[4] C. S. Peng, T. Jouhti, P. Laukkanen, E.-M. Pavelescu, J. Konttinen, W. Li, and M. Pessa, IEEE Photonics Technol. Lett. **14**, 275 (2002).

[5] J. Wei, F. Xia, C. Li, and S. R. Forrest, IEEE Photonics Technol. Lett. **14**, 597 (2002).

[6] S. Sato, Jpn. J. Appl. Phys., Part 1 **39**, 3403 (2000).

[7] M. Kawaguchi, T. Miyamoto, E. Gouardes, D. Schlenker, T. Kondo, F. Koyama, and K. Iga, Jpn. J. Appl. Phys., Part 2 **40**, L744 (2001).

[8] N. Tansu and L. J. Mawst, IEEE Photonics Technol. Lett. **14**, 444 (2002).

[9] A. Ramakrishnan, G. Steinle, D. Supper, C. Degen, and G. Ebbinghaus, Electron. Lett. **38**, 322 (2002).

[10] G. Steinle, H. Riechert, and A. Yu. Egorov, Electron. Lett. **37**, 93 (2001).

[11] E. Tournie, M.-A. Pinault, M. Laugt, J.-M. Chauveau, A. Trampert, and K. H. Ploog, Appl. Phys. Lett. **82**, 1845 (2003).

[12] D. Gollub, M. Fischer, and A. Forchel, Electron. Lett. **38**, 1183 (2002).

[13] M. O. Fischer, M. Reinhardt, and A. Forchel, IEEE J. Sel. Top. Quantum Electron. **7**, 149 (2001).

[14] M. Fischer, M. Reinhardt, and A. Forchel, Electron. Lett. **36**, 1208 (2000).

[15] J. S. Wang, A. R. Kovsh, R. S. Hsiao, L. P. Chen, J. F. Chen, T. S. Lay, and J. Y. Chi, J. Cryst. Growth **262**, 84 (2004).

[16] H. Y. Liu, M. Hopkinson, P. Navaretti, M. Gutierrez, J. S. Ng, and J. P. R. David, Appl. Phys. Lett. **83**, 4951 (2003).

[17] W. Zhou, K. Uesugi, and I. Suemune, Appl. Phys. Lett. **83**, 1992 (2003).

[18] T. Hakkarainen, J. Toivonen, M. Sopanen, and H. Lipsanen, J. Cryst. Growth **234**, 631 (2002).

[19] N. Tansu, J.-Y. Yeh, and L. J. Mawst, IEEE J. Sel. Top. Quantum Electron. **9**, 1220 (2003).

[20] N. Tansu, J.-Y. Yeh, and L. J. Mawst, Appl. Phys. Lett. **82**, 4038 (2003).

[21] W. Shan, W. Walukiewicz, J. W. Ager III, E. E. Haller, J. F. Geisz, D. J. Friedman, J. M. Olson, and S. R. Kurtz, Phys. Rev. Lett. **82**, 1221 (1999).

[22] J. Wu, W. Shan, and W. Walukiewicz, Semicond. Sci. Technol. **17**, 860 (2002).

[23] I. Vurgaftman and J. R. Meyer, J. Appl. Phys. **94**, 3675 (2003).

[24] J.-Y. Duboz, J. A. Gupta, Z. R. Wasilewski, J. Ramsey, R. L. Williams, G. C. Aers, B. J. Riel, and G. I. Sproule, Phys. Rev. B **66**, 085313 (2002).

[25] D. Alexandropoulos and M. J. Adams, IEEE J. Quantum Electron. **39**, 647 (2003).

[26] J. C. L. Yong, J. M. Rorison, and I. H. White, IEEE J. Quantum Electron. **38**, 1553 (2002).

[27] S. Tomic and E. P. O'Reilly, Physica E (Amsterdam) **13**, 1102 (2002).

[28] S. Tomic, E. P. O'Reilly, R. Fehse, S. J. Sweeney, A. R. Adams, A. D. Andreev, S. A. Choulis, T. J. C. Hosea, and H. Riechert, IEEE J. Sel. Top. Quantum Electron. **9**, 1228 (2003).

[29] Y. X. Dang, W. J. Fan, S. T. Ng, S. F. Yoon, and D. H. Zhang, J. Appl. Phys. **97**, 103718 (2005).

[30] W. J. Fan, S. T. Ng, S. F. Yoon, M. F. Li, and T. C. Chong, J. Appl. Phys. **93**, 5836 (2003).

[31] W. W. Chow, E. D. Jones, N. A. Modine, A. A. Allerman, and S. R. Kurtz, Appl. Phys. Lett. **75**, 2891 (1999).

[32] S. Ridene, K. Boujdaria, H. Bouchriha, and G. Fishman, Phys. Rev. B **64**, 085329 (2001).

[33] I. Vurgaftman, J. R. Mohan, and L. R. Ram-Mohan, J. Appl. Phys. **89**, 5815 (2001).

[34] T. B. Bahder, Phys. Rev. B **41**, 11992 (1990).

[35] C. R. Pidgeon and R. N. Brown, Phys. Rev. **146**, 575 (1966).

[36] K. Boujdaria, S. Ridene, and G. Fishman, Phys. Rev. B **63**, 235302 (2001).

[37] J. B. Xia and W. J. Fan, Phys. Rev. B **40**, 8508 (1989).

[38] W. J. Fan and S. F. Yoon, J. Appl. Phys. **90**, 843 (2001).

[39] W. J. Fan, M. F. Li, T. C. Chong, and J. B. Xia, J. Appl. Phys. **80**, 3471 (1996).

[40] J. Minch, S. H. Park, T. Keating, and S. L. Chuang, IEEE J. Quantum Electron. **35**, 771 (1999).

[41] S. Tomic and E. P. O'Reilly, IEEE Photonics Technol. Lett. **15**, 6 (2003).

[42] S.-H. Park, H.-M. Kim, W.-G. Jeong, and B.-D. Choe, J. Appl. Phys. **79**, 2157 (1996).

[43] S. A. Choulis, T. J. C. Hosea, S. Tomic, M. Kamal-Saadi, A. R. Adams, E. P. O'Reilly, B. A. Weinstein, and P. J. Klar, Phys. Rev. B **66**, 165321 (2002).

[44] E. P. O'Reilly and A. Lindsay, Phys. Status Solidi B **216**, 131 (1999).

[45] C. Skierbiszewski, Semicond. Sci. Technol. **17**, 803 (2002).

[46] B. Jogai and D. N. Talwar, Phys. Rev. B **54**, 14524 (1996).

[47] F. Szmulowicz and G. J. Brown, Phys. Rev. B **51**, 13203 (1995).

[48] C.-F. Hsu, P. S. Zory, C.-H. Wu, and M. A. Emanuel, IEEE J. Sel. Top. Quantum Electron. **3**, 158 (1997).

[49] D. J. Palmer, P. M. Smowton, P. Blood, J.-Y. Yeh, L. J. Mawst, and N. Tansu, J. Appl. Phys. **86**, 071121 (2005).

[50] C. Skierbiszewski, P. Perlin, P. Wisniewski, W. Knap, T. Suski, W. Walukiewicz, W. Shan, K. M. Yu, J. W. Ager, E. E. Haller, J. F. Geisz, and J. M. Olson, Appl. Phys. Lett. **76**, 2409 (2000).

[51] D. L. Young, J. F. Geisz, and T. J. Coutts, Appl. Phys. Lett. **82**, 1236 (2003).

[52] P. N. Hai, W. M. Chen, I. A. Buyanova, H. P. Xin, and C. W. Tu, Appl. Phys. Lett. **77**, 1843 (2000).

[53] I. A. Buyanova, W. M. Chen, and C. W. Tu, Semicond. Sci. Technol. **17**, 815 (2002).

[54] S. Tomic, E. P. O'Reilly, P. J. Klar, H. Gruning, W. Heimbrodt, W. M. Chen, and I. A. Buyanova, Phys. Rev. B **69**, 245305 (2004).

[55] A. Lindsay and E. P. O'Reilly, Phys. Rev. Lett. **93**, 196402 (2004).

[56] Y. Zhang, A. Mascarenhas, H. P. Xin, and C. W. Tu, Phys. Rev. B **61**, 7479 (2000).

[57] R. Fehse, S. Tomic, A. R. Adams, S. J. Sweeney, E. P. O'Reilly, A. Andreev, and H. Riechert, IEEE J. Sel. Top. Quantum Electron. **8**, 801 (2002).

[58] O. Gilard, F. Lozes-Dupuy, G. Vassilieff, S. Bonnefont, P. Arguel, J. Barrau, and P. Le Jeune, J. Appl. Phys. **86**, 6425 (1999).

[59] S. W. Corzine, R. H. Yan, and L. A. Coldren, Appl. Phys. Lett. **57**, 2835 (1990).

[60] J. M. Ulloa, J. L. Sanchez-Rojas, A. Hierro, J. M. G. Tijero, and E. Tournie, IEEE J. Sel. Top. Quantum Electron. **9**, 716 (2003).

[61] L. Bellaiche, S.-H. Wei, and A. Zunger, Phys. Rev. B **56**, 10233 (1997).